Title

Improving edge crystal identification in flood histograms using triangular shape crystals

Permalink

https://escholarship.org/uc/item/95v1k6vs

Journal

Biomedical Physics & Engineering Express, 4(2)

ISSN

2057-1976

Authors

Peng, Peng
Liu, Chih-Chieh
Du, Junwei
et al.

Publication Date

2018-03-01

DOI

10.1088/2057-1976/aaaa84

Peer reviewed

Improving Edge Crystal Identification in Flood Histograms Using Triangular Shape Crystals

Peng Peng[1], **Chih-Chieh Liu**[1], **Junwei Du**[1], **Xiaowei Bai**[1], and **Simon R Cherry**[1]

[1]Department of Biomedical Engineering, University of California-Davis, One Shields Avenue, Davis, CA 95616, USA

Abstract

This work presents a method to improve the separation of edge crystals in PET block detectors. As an alternative to square-shaped crystal arrays, we used an array of triangular-shaped crystals. This increases the distance between the crystal centres at the detector edges potentially improving the separation of edge crystals. To test this design, we have compared the flood histograms of two 4×4 scintillator arrays in both square and triangular configurations. The quality of the flood histogram was quantified using the fraction of events positioned in the correct crystal based on a 2D Gaussian fit of the segmented flood histograms. In the first study, the two crystal arrays were coupled with the SiPM directly using optical grease, and the flood histogram quality for the edge and corner crystals in the triangular-shaped array were much better than that for those crystals in the square-shaped array. The average light collection efficiency for the triangular-shaped array was 5.9% higher than that for the square-shaped array. The average energy resolution for the triangular and square shape array were 11.6% and 13.2% respectively. In the second study, two light guides with thickness 1 mm and 2 mm were used between the crystal arrays and the SiPM. The thicker lightguide degraded the light collection efficiency and energy resolution due to the light loss introduced by the light guide. However, in the 2-mm thick lightguide case, the flood histogram quality for the edge and corner crystals in the square-shaped array were improved due to better separation of those crystals in the flood histogram. Comparing the performance of the two crystal arrays with three different light guides, the triangular-shaped crystal array with no lightguide gave the best performance.

Keywords

PET; Detector positioning; Flood histogram

1. Introduction

Positron emission tomography (PET) is an important imaging modality for obtaining *in vivo* functional images [1]. The spatial resolution in PET is mainly determined by the dimensions of the scintillation crystals [2] in a pixelated array. The optimal method for position decoding is one-to-one coupling of crystals to photodetectors with each photodetector read out individually. Small crystal sizes are often used in preclinical PET scanners to improve spatial resolution [3]. However, as crystal size decreases, one-to-one coupling becomes very hard to implement, because of the small size of the photodetector and the large number of readout channels [4]. In this situation, optical multiplexing is often used [5]. With optical

multiplexing, light loss near the edges of the detector module degrades crystal separation, and carefully designed light guides are often needed to resolve the crystals [6]. However, light guides decrease light collection efficiency and degrade energy resolution [7].

In this paper, we investigate a method aimed at improving separation of edge crystals without decreasing light collection efficiency, using crystal elements with triangular shape cross-section. As compared to square-shaped crystal elements, triangular-shaped crystals show increased spacing between the crystal centres at the edge of the array (Figure 1). To test this design, the edge crystal separation of the triangular-shaped crystal array was compared with that of a conventional square-shaped array. The effect of adding a light guide also was investigated.

To measure the quality of the flood histogram for a PET detector, several methods have been proposed. The peak-to-valley ratio uses the ratio between the average value of the peaks and the average value of the valleys to quantify the separation of crystals in the flood histogram [4]. Another method uses the separation of the peak positions and the width of the spots to assess flood histogram quality [8]. While these two methods are suitable to use for arrays with square-shaped crystals, they are not well defined for an array with triangular-shaped crystals. In this paper, we used the crystal crosstalk matrix to evaluate the flood histogram [9]. In the crosstalk matrix method, the figure-of-merit (FOM) was defined as the fraction of events positioned in the correct crystal based on a 2D Gaussian fit of the segmented flood histograms.

After acquiring coincidence events, the quality of the flood histogram, light collection efficiency and energy resolution were calculated for each crystal in the two arrays, and the effect of light guide thickness was also studied for both arrays.

2. Materials and Methods

2.1 Crystal arrays

Two crystal arrays (Crystal Photonics Inc., Sanford, FL) were used in this study (Figure 1). One crystal array consisted of a 4×4 matrix of square-shaped LYSO crystals on a 1.34 mm pitch, and with a length of 20 mm. The other crystal array consisted of 16 triangular-shaped LYSO crystals, with length and cross section equal to the square array. The three sides for the triangular-shaped crystals measured 1.76 mm × 1.76 mm × 2.49 mm. Enhanced specular reflector (ESR) films optically separated the crystal elements.

2.2 Experimental setup

The experiments in this paper used a coincidence detection setup incorporating the test detector and a reference detector (Fig. 2a). The test detector consisted of the two crystal arrays coupled to a SensL ArrayJ-30035-16P silicon photomultiplier (SiPM) array (Figure 2b). Optical grease (BC-630, Bicron, OH) was used to couple the crystal arrays to the SiPM array. In addition to direct coupling, acrylic light guides with two thicknesses (1 and 2 mm) were also evaluated. A 3D printed frame held the two crystal arrays in alignment with the SiPM array. The reference detector module consisted of a $10 \times 10 \times 5$ mm^3 LYSO crystal coupled to a Hamamatsu H6610 photomultiplier tube (PMT).

The detectors were irradiated with a 0.68 MBq ^{22}Na point source. The summed signal from the SiPM array and the signal from the PMT were fed into two constant fraction discriminators (CFDs) (Tennelec TC453, Oak Ridge, TN) respectively, and the outputs of the two CFDs formed the coincidence trigger in the coincidence logic unit (Philips Scientific 756, Mahwah, NJ). The output signal of the coincidence unit was used to trigger the CAEN 5472 digitizer to acquire the energy and position signals from the test detector module. The setup was placed in a temperature controlled and light-tight box, and maintained at 22.0 ± 0.5°C. The SiPM over-voltage was set at 2.50 ± 0.02 V.

2.3 Readout method

Row column summing was used to reduce the number of readout channels [10]. Resistive weights (R1-16, Figure 3) were set according to the SiPM locations, yielding four position signals: X1, X2, Y1, Y2 (Figure 3). The position and energy were calculated as follows:

$$x = \frac{X1 - X2}{X1 + X2}, y = \frac{Y1 - Y2}{Y1 + Y2} \quad (1)$$

$$E = X1 + X2 + Y1 + Y2 \quad (2)$$

2.4 Analysis methods

Three features were calculated to compare the performance of the two crystal arrays: the flood histogram quality, the light collection efficiency, and the energy resolution. These values were calculated for each crystal in the two arrays.

2.4.1 Flood histograms—The crystal crosstalk matrix was used to evaluate flood histogram quality [9]. To quantify crystal separation, the flood histogram was segmented using the watershed algorithm. Each region was fit with a 2D Gaussian function to estimate crystal position, and a crystal crosstalk matrix was calculated based on the overlap of the Gaussians defined by adjacent crystals. Diagonal elements in the matrix represent the correctly positioned events, while off-diagonal elements represent mispositioned events. The FOM for each crystal is defined as the corresponding diagonal element in the crystal crosstalk matrix. However, there are regions where the histograms of several crystals are overlapping and cannot be separated in the segmentation map. For these crystals, the FOM is defined by the value of the diagonal element representing the region divided by the number of crystals in that region.

2.4.2 Calibration—Due to the non-linearity of the SiPM response, calibration is needed to get the correct 511 keV photopeak position and energy resolution [11]. To calibrate the SiPM, we used both ^{22}Na and ^{137}Cs radiation sources to obtain the ADC values for three different energies: 511 keV, 662 keV and 1275 keV (Figure 4a). The non-linearity of the SiPM can be described as [12]:

$$N_{fire} = N_{total} \cdot \left[1 - exp\left(-\frac{N_{photon} \cdot PDE}{N_{total}}\right)\right] \quad (3)$$

in which N_{fire} is the number of SiPM microcells that fire, N_{total} is the total number of SiPM microcells in one SiPM pixel, N_{photon} is the number of photons reaching the SiPM surface, and PDE is the photon detection efficiency of the SiPM. Equation (3) can be related to measured experimental quantities as follows:

$$ADC_{raw} = ADC_{max} \cdot \left[1 - exp\left(-\frac{ADC_{cal}}{ADC_{max}}\right)\right] \quad (4)$$

ADC_{raw} is the measured ADC value corresponding to the photopeak, ADC_{max} is the maximum ADC value the SiPM can output, ADC_{cal} is the ADC value assuming the photodetector response is linear. Calibration is then accomplished by inverting Equation (4):

$$ADC_{cal} = -ADC_{max} \cdot ln\left(1 - \frac{ADC_{raw}}{ADC_{max}}\right) \quad (5)$$

ADC_{max} is the only parameter in Equation (5) that is unknown and it can be estimated by fitting the data in Figure 4(b) with:

$$ADC_{raw} = ADC_{max} \cdot \left[1 - exp\left(-\frac{b \cdot E_\gamma}{ADC_{max}}\right)\right] \quad (6)$$

In Equation (6), $ADC_{cal} = b \cdot E_\gamma$ is the relationship between the output ADC value and the gamma ray energy that would be observed for a linear photodetector, where b is a scaling factor. It was found that the fitting parameter varies for different crystals (likely due to the fact that different crystals are coupled to a differing number of SiPM pixels – see Figure 1), thus the calibration was done for each individual crystal. The average calibration factor applied to convert the uncalibrated ADC data to calibrated ADC values at an energy of 511 keV was 1.062.

2.4.3 Light collection efficiency—This study was designed to compare the performance of the two crystal arrays, thus only the relative light collection efficiency, in terms of the ADC value of the 511 keV photopeak (corrected for SiPM saturation) was used. The energy spectrum was generated for each segmented region in the flood histogram. For segmented areas containing only one crystal, the energy spectrum had one 511 keV photopeak as shown in Figure 5(a). For segmented areas with two or more inseparable crystals, the energy spectrum had two or more 511 keV photopeaks as shown in Figure 5(b). The photopeak position was calibrated for each crystal one by one. Afterwards, a crystal map was generated to indicate the light collection efficiency for each crystal.

2.4.4 Energy resolution—The energy resolution was calculated as the ratio between the full width half maximum (FWHM) and central value of the 511 keV photopeak. Its value depends not only on the number of photoelectrons that are converted to electronic signals, but also on the effect of neighbouring crystals on its energy spectrum. If two crystals are inseparable in the flood histogram, the 511 keV photopeaks overlap in the energy spectrum (Figure 5(b)), and the fitting result for the two 511 keV photopeaks will affect each other. When the two photopeaks were well separated as shown in Figure 5(b), the energy resolution can still be estimated. However, if the two photopeaks were too close, it became hard to get obtain a good fit for each peak, and a single broad Gaussian fit would be used to as a measure for the energy resolution for both crystals.

2.4.5 Intrinsic detector spatial resolution—To study the effect of the crystal shape on the detector spatial resolution, we compared the intrinsic spatial resolution between two simulated scanners using the square and triangular shape crystals respectively. Gate v7.2 (Geant4 Application for Tomographic Emission) was used for the simulation [13]. The simulated scanner has two detector heads. The inner ring diameter of the scanner is 84 mm. There were 12×12 LYSO crystals in each head, the shape of the crystal was the same as described in section 2.1.

An ideal back-to-back gamma-ray point source with an energy of 511 keV was simulated at the center of the field-of-view (CFOV). Positron range and non-collinearity were not considered. The source activity was 1 MBq and the scan time was 10 seconds, ~8000 coincidence events were collected for each study.

Coincidence events from the two detector heads were collected for the intrinsic spatial resolution calculation [2]. All the true coincidences were back projected along their lines-of-response (LORs) onto the focal plane in the middle of the detector heads (YZ plane as in the Figure 6). Instead of a single line, multi-ray tracing was used to account for the detection region of each crystal pair (around 500×500 rays for each crystal pair). Owing to the irregular sampling space between triangular shape crystals, the focal plane had to be re-parameterized back into a rectangular grid. The pixel size of the focal plane was set to 0.16 mm, which is small enough to avoid under sampling of the activity distribution of the point source. The intrinsic spatial resolution was measured as the FWHM of the line profile through the center of the focal plane image of the point source after Gaussian fitting.

3. Results

3.1 Flood Histograms

To compare the performance of the two detector configurations, the crystals were grouped into centre, edge, or corner elements (Figure 7). The flood histogram quality was compared within each group.

In the first study, the crystal arrays were coupled directly to the SiPM array. The 0.35 mm glass window covering the SiPM surface was sufficient to position crystals in the triangular-shaped array without the need for an additional light guide.

To quantify the quality of the flood histogram, the FOM was calculated as defined in Section 2.4.1. As shown in Figure 9, the corner crystals in both arrays show the lowest FOM, and are not separable. Comparing Figure 7 with Figure 1, we notice that the corner group in the triangular-shaped array has two crystals in each segmented area, the edge group in the square-shaped array has two crystals in each segmented area, and the corner group in the square-shaped array has four crystals in each segmented area.

Without a light guide, the edge crystals were resolved when using the triangular-shaped crystal array, but were not resolved when using the square-shaped crystal array.

3.2 Light collection efficiency

Light collection was evaluated separately for corner, edge, and centre crystals. The amplitude of the 511 keV photopeak is shown in Figure 10. The outermost crystals generally show the lowest light collection, as do crystals which sit over gaps between SiPM elements. The triangular array shows higher light collection efficiency than the square array, with 6.3%, 1.5% and 12.4% higher values for the centre, edge and corner crystals respectively. The average improvement for all crystals was 5.9%.

3.3 Energy Resolution

For the triangular array, there was no clear correlation between energy resolution and position (Figure 11). For square arrays, the energy resolution was degraded towards the detector edge. The triangular shape array had a better average energy resolution of 11.6% compared to the square shape array, which had an average energy resolution of 13.2%.

3.4 Light Guide Thickness

Acrylic light guides were used to increase light sharing on the photodetector and improve crystal separation. 1 and 2 mm light guides were tested, with corresponding flood histograms shown in Figure 12. Increasing light guide thickness causes blurring of the peaks in the flood histogram. The 2 mm light guide allowed for separation of the outermost crystals for the square array, yielding a sharp increase in flood histogram quality. However, increasing the thickness of the light guide decreased the overall light collection, as shown in Figure 13(b).

The dependence of energy resolution on light guide thickness was more complicated. As the light guide became thicker, the lower light collection efficiency degrades the energy resolution. On the other hand, the thicker light guide helped in separating the crystals in the flood histogram, which improves the energy resolution. There was no clear trend in Figure 13(c) between the energy resolution and the thickness of the light guide.

Figure 13 shows that for the triangular-shaped array, performance was best without a light guide. Comparable performance with the square-shaped array was only achieved when using a 2 mm light guide.

In Table 1, we compared the performance of the two crystal arrays using the optimal light guide for each configuration. The triangular crystal array outperformed the square-shaped array across the majority of parameters.

3.5 Intrinsic detector spatial resolution

The intrinsic detector spatial resolution defined in section 2.4.5 was studied for scanners simulated with both square shape and triangular shape crystals. The focal plane image of the point source from the two scanners using square and triangular shape crystals is shown in Figure 14.

The point source was placed at different locations on the focal plane. An average intrinsic spatial resolution was calculated and the FWHM values are shown in Table 2.

The average spatial resolution for the scanner using square shape crystals is slightly better than that for the scanner using triangular shape crystals.

4. Discussion and Conclusions

In this paper, we described a method to improve the separation of edge crystals in PET detector modules using triangular-shaped crystal elements.

In the first study, we coupled the two crystal arrays with triangular and square shape crystals directly to the photodetector without a light guide. The performance of the two crystal arrays was compared in terms of the flood histogram quality, the light collection efficiency, and the energy resolution. The triangular-shaped crystal array had better performance in all three parameters as shown in Figures 9–11. In the second study, we used two acrylic light guides with thicknesses of 1 mm and 2 mm, and studied the effect on the performance of the two crystal arrays. As shown in Figure 13, the three performance parameters became worse as the light guide became thicker for the triangular shape crystal array. However, for the square shape crystal array, when the lightguide was 2 mm thick, the flood histogram quality and energy resolution improved relative to the 0 and 1 mm cases. This confirms the results of previous studies showing the benefit of light guides for square shape crystal arrays. However, as shown in Table 1, the triangular shape crystal array with no light guide has better performance than the square shape crystal array with 2 mm lightguide, especially in terms of light collection efficiency.

The cost of the triangular shape crystal using current methods is twice the price for the square shape crystal with the same volume, because the vendor started with a regular square pixel and then ground half of the volume away to make it triangular. This process is wasteful. However, if the triangular shape crystal is cut directly from the scintillator boule, or if a ceramic scintillator is used, the cost and yield can be improved and there is no reason for any significant cost discrepancy between the two shapes.

The effect of crystal shape on the detector intrinsic spatial resolution was studied using GATE simulation. On average, the spatial resolution for the square crystal scanner is 1.03 mm along both y and z axes, and is 1.15 mm along both y and z axes for the triangular crystals. The square crystal scanner has slightly better performance in terms of spatial resolution. However, the difference might be partially compensated when coincidence events from all projection angles in a full ring system are used in the image reconstruction, and the

difference may also be reduced in a real detector where positron range and non-collinearity will somewhat degrade intrinsic resolution.

The use of triangular shape crystal array with no light guide may be beneficial in obtaining good timing resolution for two reasons. First, the higher light collection efficiency will improve the timing resolution [14]. Second, the removal of the light guide will eliminate additional path length dispersion induced by the light guide, which will improve the timing resolution [15]. The timing resolution will be studied in the next phase of this development work.

Acknowledgments

References

1. Cherry R MS. In vivo molecular and genomic imaging: new challenges for imaging physics. Phys Med Biol. 2004; 49:R13–R48. [PubMed: 15012005]

2. Moses WW. Fundamental Limits of Spatial Resolution in PET. Nucl Instr Meth Phys Res A. 2011; 648:S236–S240.

3. Goertzen AL, et al. NEMA NU 4-2008 Comparison of Preclinical PET Imaging Systems. J Nucl Med. 2012; 53:1300–1309. [PubMed: 22699999]

4. Chatziioannou A, Tai YC, Doshi N, Cherry SR. Detector development for microPET II: a 1 μl resolution PET scanner for small animal imaging. Phys Med Biol. 2001; 46:2899–2910. [PubMed: 11720354]

5. Lewellen TK. Recent developments in PET detector technology. Phys Med Biol. 2008; 53:R287–R317. [PubMed: 18695301]

6. Gu Z, Prout DL, Valenciaga Y, Chatziioannou AF. Lightguides for improving edge crystal identification and energy resolution in pixelated scintillator. IEEE NSS/MIC; San Diego, CA, USA: 2015.

7. Raylman RR, Majewski S, Mayhugh MR. Light sharing in multi-flat-panel-PMT PEM detectors. Physica Medica. 2006; 21:83–86. [PubMed: 17646002]

8. Du JW, et al. A Simple Capacitive Charge-Division Readout for Position-Sensitive Solid-State Photomultiplier Arrays. IEEE Trans Nucl Sci. 2013; 60(5):3188–3197. [PubMed: 25558081]

9. Xia T, , et al. Fast and Accurate Detector Module Crystal Blur and Mis-position Error Modeling for PET Imaging. IEEE NSS/MIC; Seattle, WA, USA: 2014.

10. Du JW, et al. Characterization of Large-Area SiPM Array for PET Applications. IEEE Trans Nucl Sci. 2016; 63(1):8–16. [PubMed: 27182077]

11. Burr KC, Wang GC. Scintillation Detection Using 3 mm × 3 mm Silicon Photomultipliers. IEEE NSS/MIC; Honolulu, HI, USA: 2007.

12. Gruber L, Brunner SE, Marton J, Suzuki K. Over saturation behavior of SiPMs at high photon exposure. Nucl Instr Meth Phys Res A. 2014; 737:11–18.

13. Jan S, et al. GATE: a simulation toolkit for PET and SPECT. Phys Med Biol. 2004; 49(4543–4561)

14. Lecoq P, et al. Factors Influencing Time Resolution of Scintillators and Ways to Improve Them. IEEE Trans Nucl Sci. 2010; 57(5):2411–2416.

15. Conti M. Focus on time-of-flight PET: the benefits of improved time resolution. Eur J Nucl Med Mol Imag. 2011; 38:1147–1157.
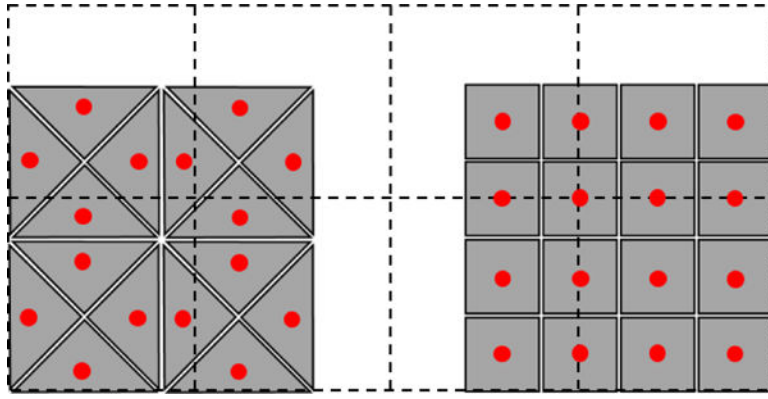
Figure 1.
Schematic for the two crystal arrays and their location on the photodetector array. The left side shows the triangular-shaped crystal array, the right side is the square-shaped crystal array. The red dot is the geometric centre for each crystal. The black dashed squares indicate the positions of the photodetector pixels.
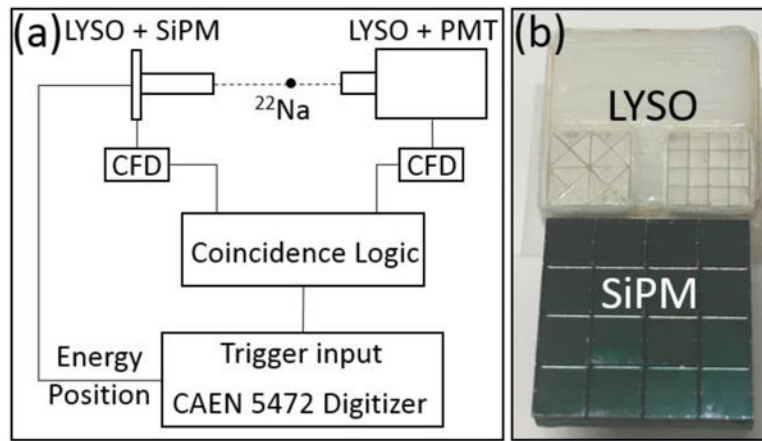
Figure 2.
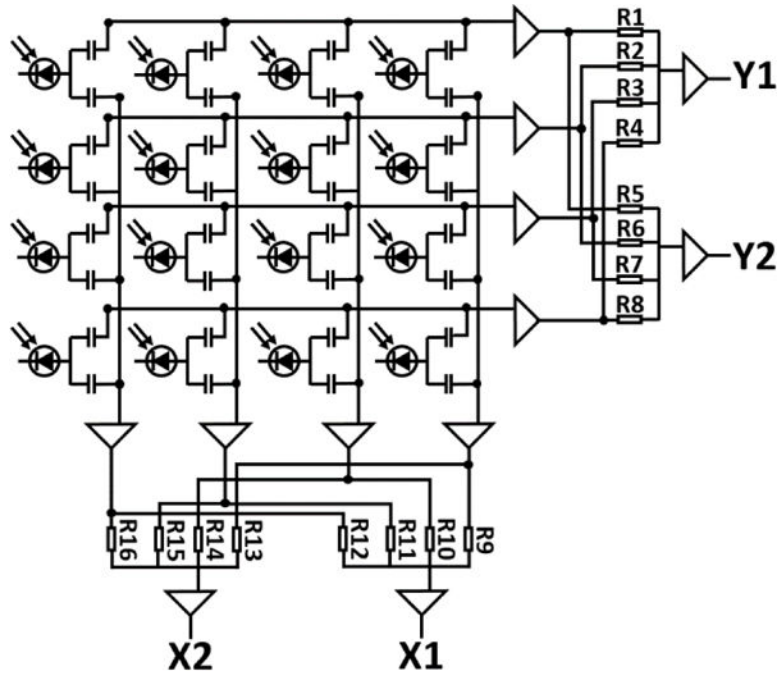(a) Experimental setup. (b) Photos of the two LYSO arrays inside a 3D printed frame and the SensL SiPM array.

Figure 3.
Schematic of the readout method.
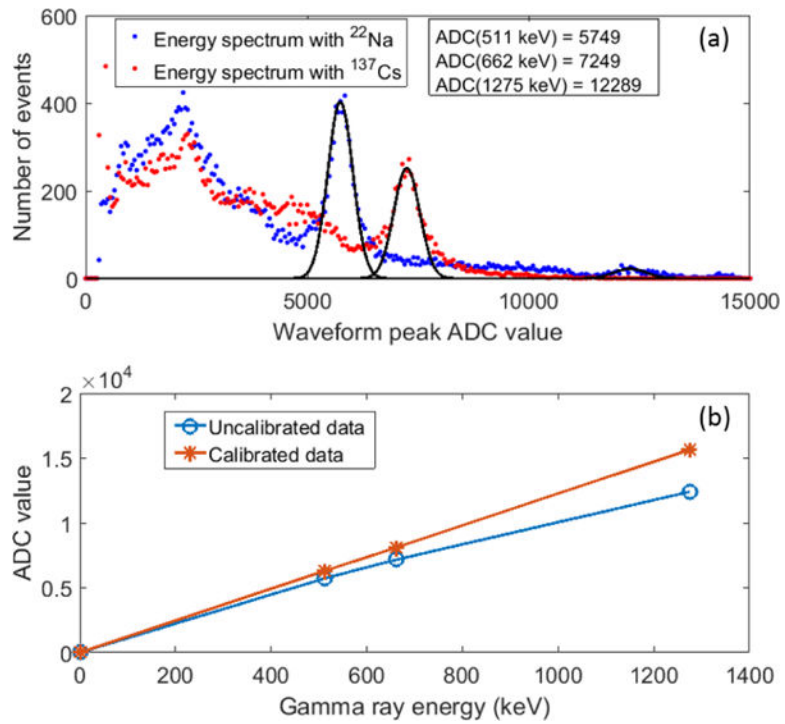
Figure 4.
(a) Energy spectra from ^{22}Na and ^{137}Cs showing the three gamma ray peaks at 511, 622 and 1275 keV. (b) Uncalibrated ADC values for these three different energies and the ADC values calibrated using Equation (5).
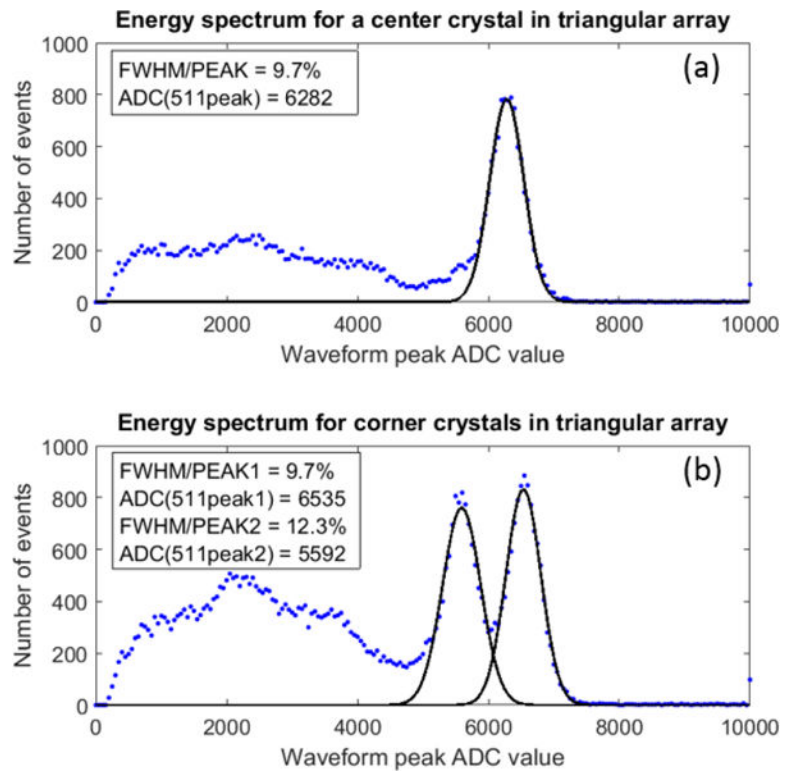
Figure 5.
(a) Energy spectrum for a segmented area containing one centre crystal. (b) Energy spectrum for a segmented area containing two corner crystals.
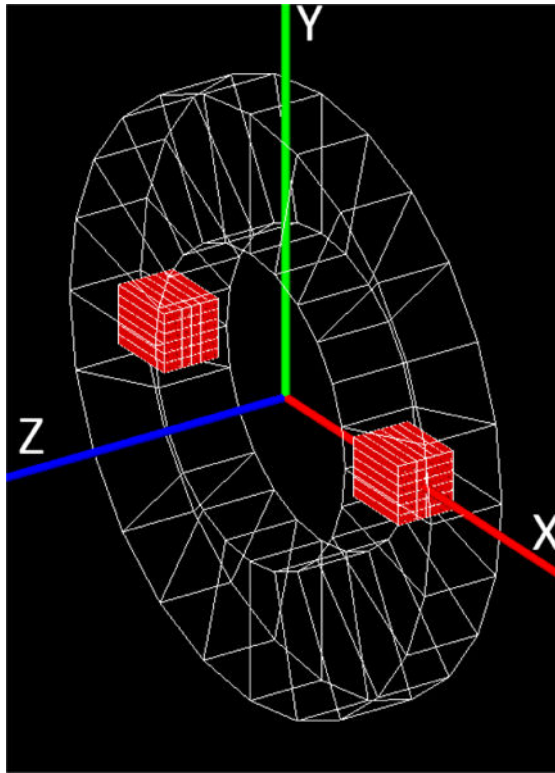
Figure 6.
Schematic plot for the simulated scanner.
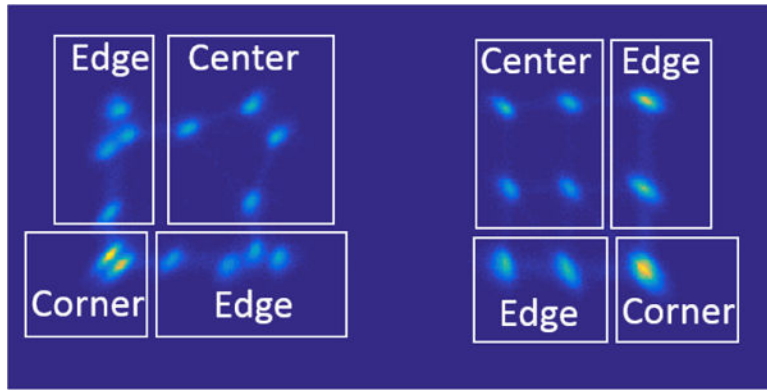
Figure 7.
Flood histogram for the two crystal arrays measured without a light guide between the crystal arrays and the SiPM array. The triangular-shaped crystal array is on the left and the square-shaped array is on the right.
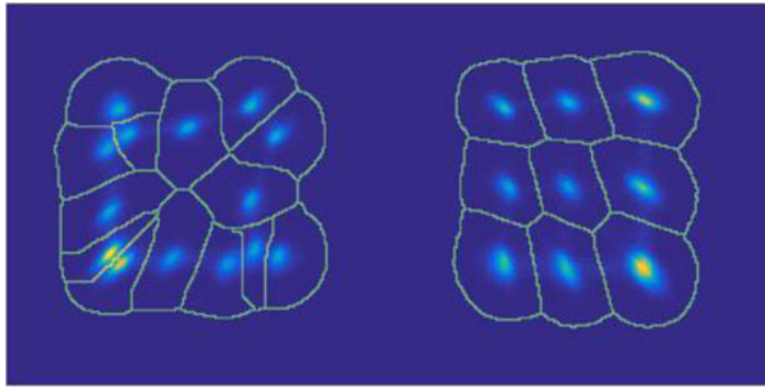
Figure 8.
Segmented flood histogram. The triangular-shaped crystal array is on the left and the square-shaped array is on the right.
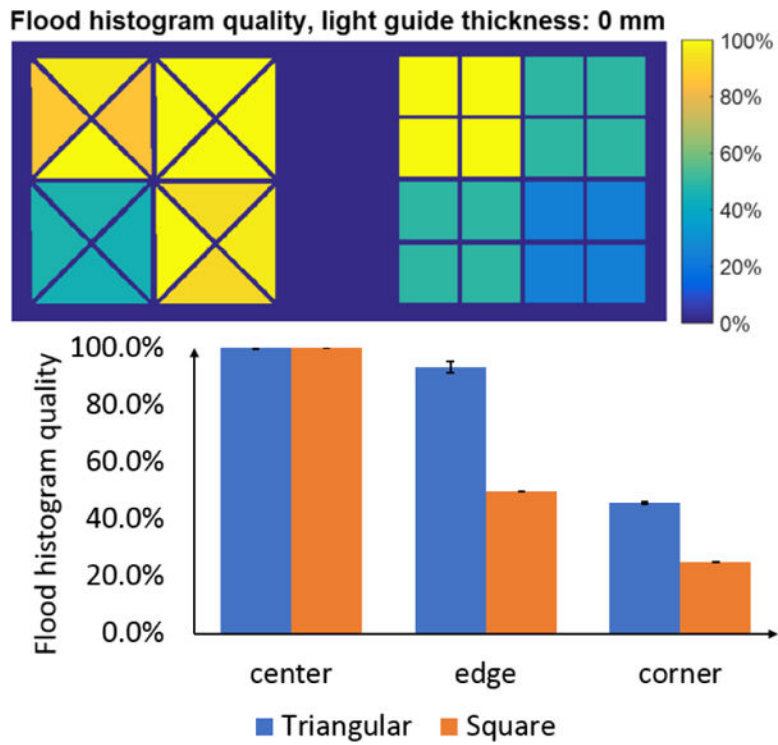
Figure 9.
Top: Flood histogram quality for each crystal in the two crystal arrays. Bottom: Average flood map quality of the two crystal arrays for the three groups of crystals.
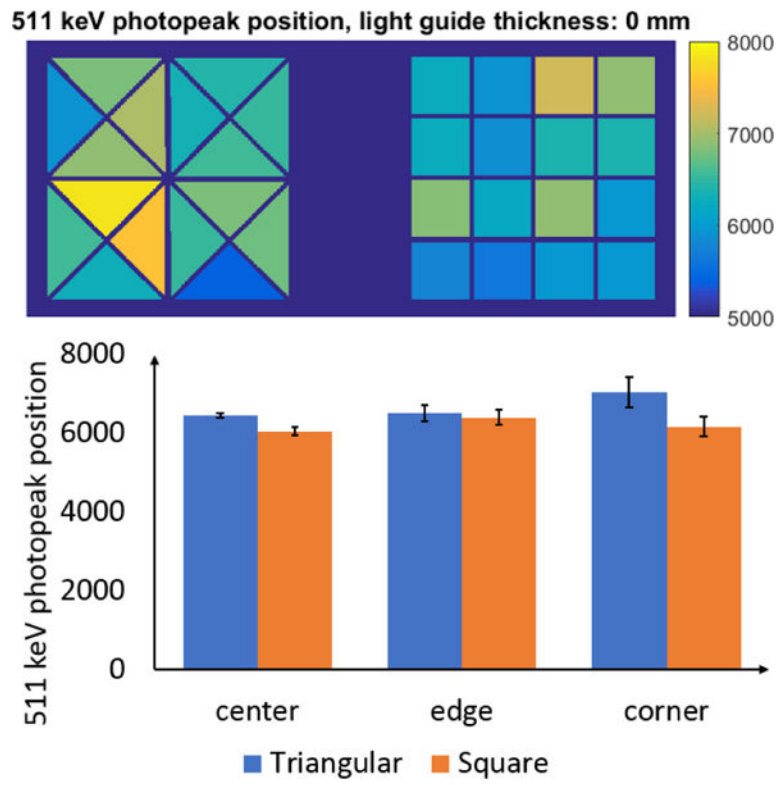
Figure 10.
Top: 511 keV photopeak position for each crystal in the two arrays. Bottom: Average values
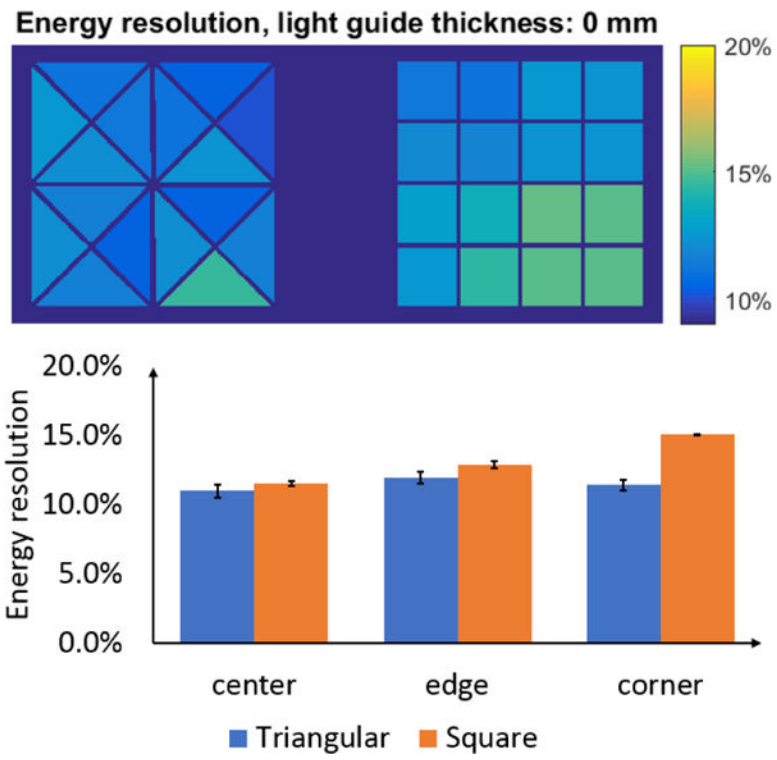for the 511 keV photopeak position in the three crystal groups.

Figure 11.
Top: Energy resolution for each crystal in the two arrays. Bottom: Average values for the energy resolution in the three crystal groups.
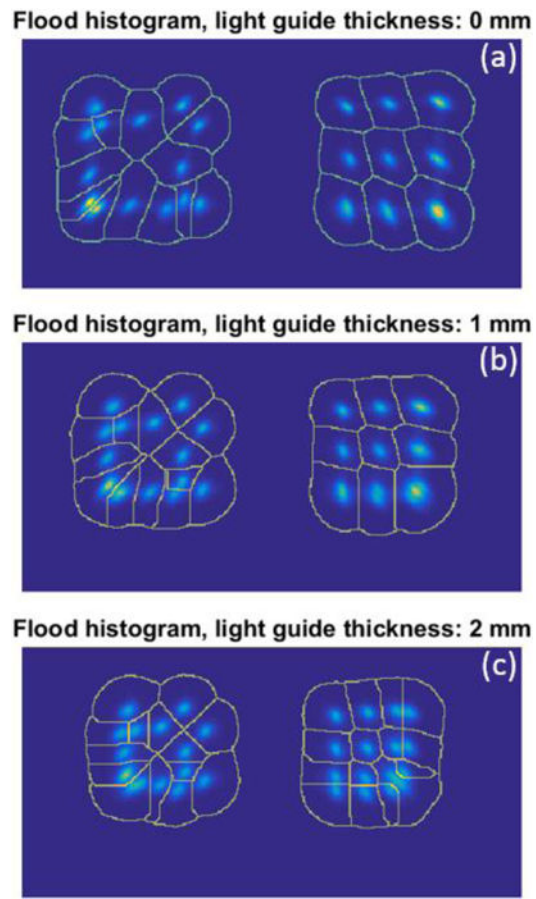
Figure 12.
Segmented flood histograms for three different light guide thicknesses: (a) 0 mm, (b) 1 mm, (c) 2 mm.
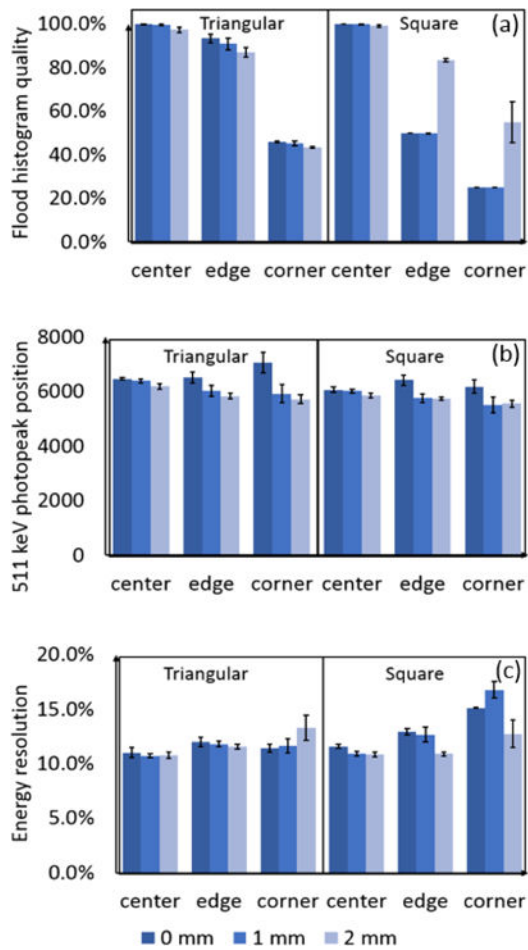
Figure 13.
Performance of the two crystal arrays for three different light guide thicknesses ranging
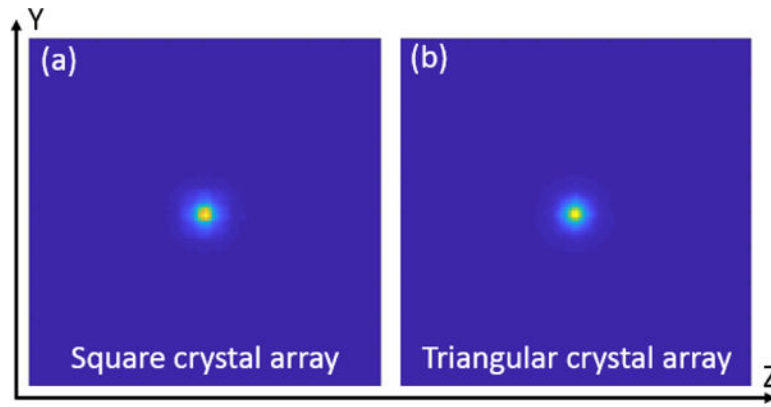from 0 to 2 mm: (a) Flood histogram, (b) 511 keV photopeak position, (c) energy resolution.

Figure 14.
Focal plane images for a simulated point source in the center of the scanner. (a) is from the square shape crystal scanner, (b) is from the triangular shape crystal scanner.

Table 1

Comparison of performance between the triangular shape crystal array with no light guide and the square shape crystal array with 2 mm thick light guide. Blue boxes indicate better performance.

Crystal shape		Triangular	Square
Light guide thickness		**0 mm**	**2 mm**
Flood histogram quality	Centre	100%	99.0%
	Edge	93.4%	83.4%
	Corner	45.8%	55.0%
511 keV photopeak ADC value	Centre	6468	5847
	Edge	6514	5734
	Corner	7056	5555
Energy resolution	Centre	11.0%	11.0%
	Edge	12.0%	10.9%
	Corner	11.5%	12.8%

Table 2

Comparison of the intrinsic spatial resolution between the scanners using square shape crystals and triangular shape crystals.

Average intrinsic spatial resolution	y (mm)	z (mm)
Square crystal	1.03	1.03
Triangular crystal	1.15	1.15